Scientific Reports

https://doi.org/10.1038/s41598-026-47481-y

Article in Press

Defined pulsed electro-magnetic field exposure suppresses stemness and potentiates temozolomide-induced apoptosis in glioblastoma cells

Received: 26 November 2025

Accepted: 31 March 2026

Published online: 09 April 2026

Cite this article as: Gullà L., Ferraro A., Gervino G. *et al.* Defined pulsed electro-magnetic field exposure suppresses stemness and potentiates temozolomide-induced apoptosis in glioblastoma cells. *Sci Rep* (2026). https://doi.org/10.1038/s41598-026-47481-y

Lorena Gullà, Angelo Ferraro, Gianpiero Gervino, Fabio Truc, Massimo Balma, Giulia Pinton & Laura Moro

Defined Pulsed Electro-Magnetic Field Exposure Suppresses Stemness and Potentiates Temozolomide-Induced Apoptosis in Glioblastoma cells

Lorena Gullà[1,2], Angelo Ferraro[3], Gianpiero Gervino[4], Fabio Truc[4,5], Massimo Balma[6], Giulia Pinton[1*], Laura Moro[1*]

[1]Department of Pharmaceutical Sciences, University of Eastern Piedmont, Novara, Italy.

[2]Laboratory of Cellular Biochemistry and Molecular Biology, Catholic University of the Sacred Heart, Milan, Italy.

[3]School of Electrical and Computer Engineering, National Technical University of Athens, Athens, Greece;

[4]Department of Physics, University of Turin, Turin, Italy;

[5]Valle D'Aosta Oncologic Foundation, Aosta, Italy;

[6]Ethidea Srl, Mathi (Turin), Italy.

*Corresponding authors:

Prof. Laura Moro

Prof. Giulia Pinton

Dipartimento di Scienze del Farmaco

Università degli Studi del Piemonte Orientale

Lgo Donegani 2, 28100 Novara – Italy

Tel. +39.0321.375820

Mail: laura.moro@uniupo.it

giulia.pinton@uniupo.it

Abstract

Glioblastoma is a highly aggressive brain tumor with rapid growth and poor prognosis, highlighting the need for novel therapeutic approaches. This study investigated the effects of defined low-frequency pulsed electromagnetic fields (PEMFs) on glioblastoma cells, focusing on cell viability, stemness, and drug response. Our findings demonstrate that daily exposure to a defined PEMF sequence over four days, slightly reduced cell viability while significantly downregulated the expression of *POU5F1* and *NANOG*. Functionally, PEMF treatment inhibited neurosphere formation, significantly decreasing both their number and size. Furthermore, *CDH1* expression was induced, while *CD44* and *ALDH1A3* expression remained unchanged, suggesting a partial mesenchymal-to-epithelial transition. Importantly, PEMF exposure enhanced the pro-apoptotic effects of the standard chemotherapeutic agent temozolomide (TMZ). Since activation of the AKT pathway is associated with resistance to TMZ, the impact of PEMF treatment on AKT activation was examined. PEMFs suppressed stemness-related gene expression without altering AKT protein levels or its phosphorylation. Notably, combining PEMF treatment with the AKT inhibitor MK-2206 caused a marked decrease in cell viability. Overall, these findings demonstrate that a precisely defined PEMF protocol selectively impairs glioblastoma cell plasticity and stem-like traits, providing a foundation for future studies into the underlying mechanisms.

Introduction

Glioblastoma (GBM) represents the most aggressive and lethal primary brain tumor in adults, characterized by rapid cellular proliferation, diffuse infiltration, and marked resistance to current therapeutic modalities [1-3]. Despite advances in surgical techniques and the development of multimodal treatment strategies, including maximal safe resection followed by radiotherapy in combination with the alkylating agent Temozolomide (TMZ), patient outcomes remain dismal. The median overall survival following standard-of-care treatment is approximately 12 to 15 months, with a 5-year survival rate of less than 10% [4-6]. A critical barrier to therapeutic success is the presence of glioma stem cells (GSCs), a subpopulation of tumor-initiating cells capable of self-renewal, multilineage differentiation, and propagation of tumor heterogeneity [7]. GSCs have been shown to exhibit intrinsic resistance to conventional therapies and are believed to play a central role in tumor recurrence and disease progression [8]. Therefore, targeting GSCs represents a pivotal focus in the development of more effective and durable treatment strategies for GBM. Recent studies have shown that promoting GSCs differentiation can enhance treatment efficacy and improve patient outcomes [9]. The presence of stem cell-like phenotypes implies the presence of molecular networks governing them. Several studies have detected the expression of pluripotency-associated markers such as OCT4, NANOG, and SOX2 in human tumors [10]. OCT4 and NANOG are homeobox transcription factors and SOX2 is a member of the Sox (SRY-related HMG box) gene family, which encodes transcription factors with a single HMG DNA binding domain. Downregulation of OCT4 and NANOG *in vitro* may allow the entry of undifferentiated cells into differentiation pathways [11,12].

A growing body of evidence indicates that GBM frequently exhibits hyperactivation of the phosphatidylinositol 3-kinase (PI3K)/AKT signaling pathway, with endogenous AKT kinase activity often induced in response to clinically relevant concentrations of TMZ [13]. Activation of AKT has been closely associated with enhanced tumorigenicity, invasiveness, and stem cell-like properties in GBM cells [14], while overexpression of constitutively active AKT has been shown to confer resistance to TMZ-mediated cytotoxicity [15]. Notably, suppression of the PI3K/AKT pathway has been demonstrated to potentiate the cytotoxic effects of TMZ [16-19]. Collectively, emerging data underscore the pivotal role of PI3K/AKT signaling in regulating the self-renewal capacity of GSCs and driving tumor progression [20,21]. Further studies are required to fully decipher the complete AKT-OCT4 interplay system in GSCs, which may be useful in revealing the intrinsic connection between self-renewal and the tumorigenesis of those cells, and in developing more effective interventions to eradicate or inhibit them.

Recent studies have explored non-invasive strategies aimed at reducing stemness through physical stimuli rather than pharmacological or genetic manipulation [22-25]. Among these, pulsed electromagnetic field (PEMF) therapy has emerged as a novel tool capable of influencing cellular behavior without direct chemical or surgical intervention [26]. Originally developed for musculoskeletal applications, PEMFs have been explored as non-thermal modulators of cellular programs in oncology and regenerative medicine, with reports of parameter-specific “windows” (frequency, intensity, waveform) associated with changes in proliferation, differentiation and inflammatory signaling [23–28]. PEMF treatment operates by radiating cells with electromagnetic fields at specific frequencies and waveform parameters to stimulate biological responses [27,28].

Although the precise mechanisms underlying PEMF-induced cellular effects remain to be fully elucidated, several hypotheses have been proposed [29]. At weak, low magnetic field amplitudes (μT), interaction models emphasize time-varying magnetic induction and the resulting electric fields that can bias ion and charge motion, membrane processes [30], electroconformational coupling (ECC) concepts and coherent/collective modes that may provide frequency selectivity without thermal dosing [31-34]. Additional proposals include voltage-gated Ca^{2+} channel (VGCC) involvement as a plausible biophysical interface for weak fields and downstream Ca^{2+} signaling cascades [35]. Concerning anti-cancer applications, Pasi et al. demonstrated that PEMF in combination with TZM induced in GBM cells transcriptional shifts consistent with enhanced apoptosis, potentially involving miRNA downregulation [36]. In other cellular contexts, radioelectric exposures have been shown to modulate stemness programs through cell polarity and reactivation of HAS2 (type 2 hyaluronan synthase). Hyaluronan dependent regulation of Bmi1/OCT4/SOX2/NANOG as well as telomerase are able to promote neurogenic commitment with antiproliferative effects [37,38]. In parallel, studies at higher magnetic intensities implicated mitochondrial checkpoints and ROS-linked oncolysis [39-41]. Recently, our group demonstrated that exposure to defined low-frequency PEMF sequences promoted differentiation of the U937

promonocytic human cell line [42]. This effect was sequence-dependent because small frequency deviations (average 5.0%) abolished the biological response, suggesting that precise signal parameters may be critical for eliciting functional changes. PEMF treatment had the ability to induce expression and activity of the chromatin remodelling factor KDM6B. Interestingly, chromatin architecture is of paramount importance during stem cell differentiation as it regulates the accessibility of genomic regions to transcription factors or other regulatory proteins [43]. The primary objective of the present study was to evaluate the effects of exposure to two specific PEMF sequences designed to operate in a non-thermal regime (XR-BK11 vs XR-BK11/F), on human GBM *in vitro* cell models, and testing their impact on stemness-related genes. Additionally, the study aimed to investigate the potential synergistic effects of PEMF in combination with TMZ, a standard chemotherapeutic agent widely used in the clinical management of GBM.

Results

Design of the PEMF sequences

It is well known that biomolecular systems respond to stimuli over time scales spanning several octaves, rather than on a single limited range; this is the reason why biological spectra are typically studied on logarithmic axes. In dielectric spectroscopy of tissues, step-like dispersions arise because different polarization mechanisms become active as stimulus frequency increases: the α-dispersion, ranging from 10 to 10^4 Hz reflects ionic and interfacial processes, whereas the β-dispersion, ranging from 10^4 to 10^7 Hz, is dominated by Maxwell–Wagner charge accumulation at cell membranes. At higher-frequencies, δ and γ dispersions involve bound and bulk water, respectively [44].

The development of the XR-BK11 PEMF sequence was based on a theoretical and experimental framework that integrates elettromagnetics and cellular dynamics. The interaction concept is inspired by models of mechanical resonance and temporal synchronization, where external signals matching the intrinsic oscillatory frequencies of a system can modulate its behaviour without direct chemical or thermal interference. This idea echoes early biophysical theories proposed by H. Fröhlich, who suggested that biological systems under non-equilibrium conditions may support coherent vibrational modes that are selectively sensitive to weak electromagnetic fields acting at resonant frequencies [31,32]. This framework motivates a PEMF frequency design that samples the α and β dispersion windows using a discrete set of base carrier frequencies and their corresponding harmonics.

The general frame of SynthéXer [42] signal (1) is based on a series of N wave segments that has been referred to as specific time sequence S(t):

$$S(t) = \sum_{i=1}^{N} A_i \; X_i(t) \, \mathrm{Rect}\left[\frac{t - \sum_{p=1}^{i-1} \Delta_p + \Delta_i/2}{\Delta_i}\right] \qquad (1)$$

where A_i is the amplitude of the signal into the segment i, X_i (t) represents the i-th waveform with its relevant parameters and Δ_i is the time duration of the i-th segment. Within each segment, several well-defined parameters such as frequency, waveform, modulation and level were therefore applied, as shown in Figure 1A. The frequencies of α-dispersion overlap slow, ion-mediated and interfacial processes but also intersects the natural stepping rates of molecular motors and cytoskeletal remodeling cycles (10^1- 10^2 s^{-1} in many contexts), which can drive coherent mechanical oscillations of elastic filaments via follower-force instabilities such as Hopf bifurcations at characteristic frequencies set by motor forcing, filament elasticity, and viscous drag. The β-dispersion samples Maxwell–Wagner membrane physics and interfacial polarization on cell-scale structures (10^4-10^7 Hz) and encompasses kHz-scale molecular stepping rate upper bounds evident in fast biosynthetic machines such as bacterial replisomes (~ 750 -1000 nt s^{-1}), which we use not as a specific claim applicable directly on glioma cells but as a biological pace-setter indicating that kHz-rate elementary transitions are feasible in living systems. To ensure a broad and coherent coverage of the electromagnetic spectrum relevant to biological systems, the XR-BK11 sequence was designed starting around a logarithmic scale based on octaves. This approach is consistent with known biophysical principles, where many biological responses are sensitive to changes in logarithmic progression. An octave represents a doubling of frequency, a concept widely adopted in physics, acoustics, neuroscience, etc. With the choice for 40 Hz as base frequency, for a range of 10 kHz, we defined 9 frequency values (2) according to the following progression:

$$f_i = 40 \times 2^{(i-1)};\ i = 1 \text{ to } 9 \qquad (2)$$

To maximize spectral reach and impulsive drive of S(t) (1) we used 50% duty cycle, square waves as waveform. This kind of stimulus, when projected into the frequency domain, produces several odd harmonics with amplitudes decaying as 1/n. Thus, each chosen base carrier at f_0 frequency, injects power also at $3f_0, 5f_0, \ldots$, rapidly densifying the spectrum across the whole range. In addition, because the rise/fall time of magnetic pulses delivered by SynthéXer device is shorter than 1 µs, the frequency-domain drive is broadband and substain a large order of harmonic series. In mechanical terms, that is equivalent to the approach to sharply excite a system to reveal its eigenstates: a sudden broadband stimulus can be used to efficiently induce fundamental and harmonic responses of damped, nonlinear targets (as expected in viscoelastic cytoplasm). The rationale for biology is twofold: (i) the base frequencies interrogate α-dispersions directly; (ii) their odd harmonics and intermodulations products provide a carpet of additional electromagnetic tones that can couple to narrower band mechano-electrical modes in β-dispersions regime. Our square-wave stimulus generates at least 10 effective spectral components per base frequency, that are first 10 odd harmonics, transforming narrowband magnetic inputs into broadband electromagnetic impulses.

A key point we considered in signal design, is to avoid harmonic overlap: the harmonics can lead to spectral superposition, where harmonics from lower frequency components overlap with higher fundamental or harmonics tones providing redundant stimulation and reducing the diversity of frequency-specific bioeffects. Moreover, less uniform energy distribution could impact the interaction efficacy with biological systems. To avoid these risks, further modifications were made where certain frequency values derived from the octaves were adjusted to maximise spectral coverage and reduce overlap. In addition, pairs of closely spaced frequencies were included on the basis of previous *in vitro* experience [42]. These adjustments are consistent with the physical and biological aim of producing a rich, non-redundant, broadband spectrum capable of interacting with different molecular and cellular targets. By means of described process, eleven base frequencies have been defined as: 40, 150, 230, 490, 720, 780, 1830, 5100, 7500, 8000, 10000 Hz, so that in the experiments herein reported, the XR-BK11 sequence was formed by a series of these N = 11 wave segments, each lasting 5 minutes, for a total duration of 55 minutes. The signal segment amplitudes Ai were chosen to drive non-thermal effects. Magnetic flux density associated with the XR-BK11 sequence segments is shown in Figure 1B.

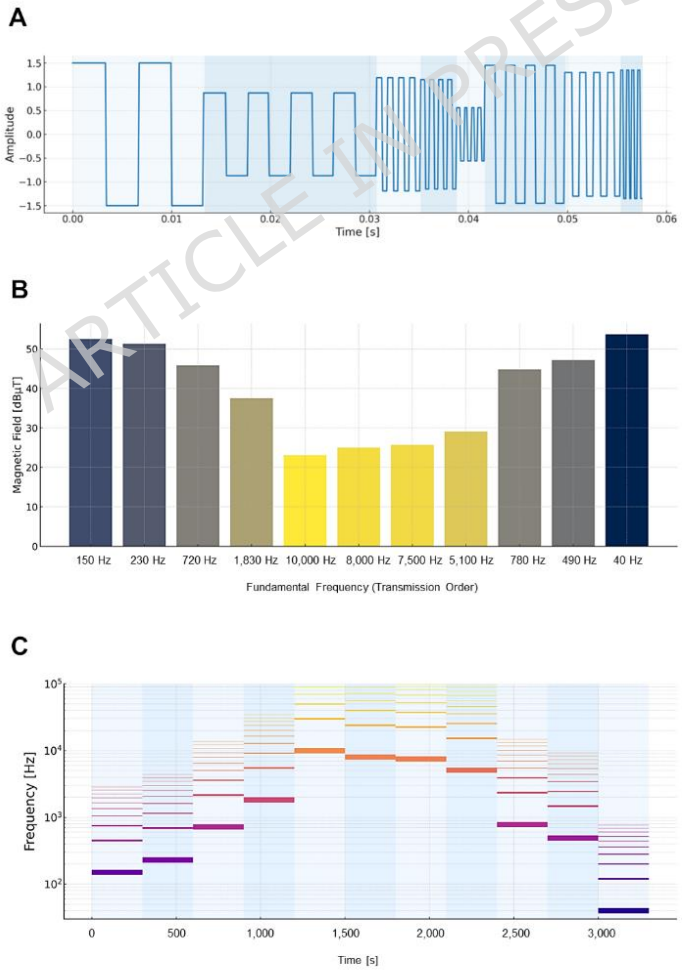

Figure 1. Magnetic flux density associated with the XR-BK11 sequence segments and set of frequencies emitted during the 55-minute. (A) The general frame of SynthéXer signal is based on a series of N wave segments (N = 8 into the picture) where every segment holds a specific duration time. Within each segment several technical parameters such

as frequency, waveform Xi, modulation and amplitude Ai are defined. **(B)** Measured magnetic field flux amplitude is shown versus the segment frequencies of the XR-BK11 sequence. The frequencies of the segments are sorted in order of emission. **(C)** This waterfall-like representation illustrates the complete set of frequencies emitted during the 55-minute XR-BK11 sequence, highlighting both the temporal and spectral distribution of the signal. Colour intensity and line thickness encode the frequency and harmonic rank, enhancing the visual perception of spectral density and structural coherence. This representation emphasizes how XR-BK11 systematically activates specific spectral bands over time, covering the biologically relevant α and β dispersion zones.

The bar plot displays the magnetic field intensity (in μT) corresponding to each of the 11 emission segments, ordered according to their temporal deployment, the first being 150 Hz, the last 40 Hz. Field values were derived by measurements at the specific fundamental frequencies of each segment. The vertical scale is logarithmic to reflect the broad range of field intensities used across the spectrum. The rapid time-varying magnetic fields of S sequence (1) induce on the cell culture predictable, weak E electric fields (3) via Faraday's law:

$$E = \omega r_C \frac{B}{2} \qquad (3)$$

where ω is the field angular frequency, r_C the cell radius and B the value of generated magnetic field. The peak values of this magnetically induced electrical field E fell in the μV/m range, at the frequencies and magnetic flux generated with XR-BK11 sequence as reported in Figure 1C.

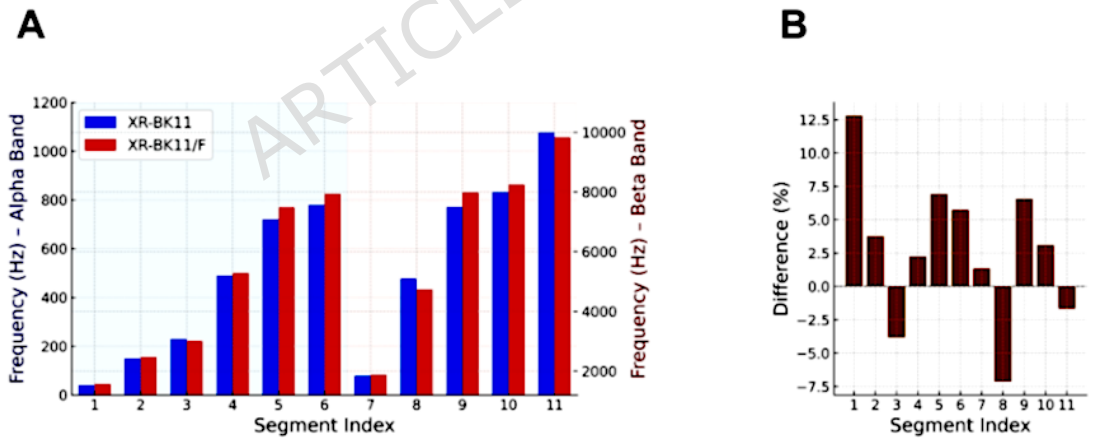

Figure 2. Comparison between XR-BK11 and XR-BK11/F frequences. (A) The bar plot shows the absolute frequencies used in the XR-BK11 sequence and its modified version XR-BK11/F, distributed across 11 time segments. Segments 1-6 correspond to the α/dispersion band (highlighted in blue background), while segments 7-11 harmonics fall within the β/dispersion band (highlighted in red background). **(B)** The plot illustrates the relative percentage differences between corresponding frequencies in the two sequences. Overall, the XR-BK11/F set maintains a close alignment to the original frequencies, with a mean deviation of 4.0% and a root-mean-square deviation of 4.3%. This visual comparison confirms that the XR-BK11/F sequence introduces only minor frequency shifts while preserving the broad spectral structure of the original sequence.

The complete set of frequencies emitted during the 55-minute XR-BK11 sequence, highlighting both the temporal and spectral distribution of the signal is shown in Figure 2. This representation emphasizes how XR-BK11 systematically activates specific spectral bands over time, covering the biologically relevant α and β dispersion zones. Each horizontal line in Figure 2A corresponds to a discrete frequency component active during one of the 11 segments, with harmonics (odd only) up to the 10^{th} order shown for each base frequency. The vertical axis is logarithmic, reflecting the wide spectral coverage of the sequence from 40 Hz to 100 kHz.

As final point in order to assess the signal specificity, a second SynthéXer sequence was designed and named XR-BK11/F. Starting from the assumption that magnetic field interaction efficacy should be frequency related to cellular phenomena timing, the only parameter variation that we introduced into XR-BK11/F was the frequency of square waves $X_i(t)$. Figure 2A shows frequencies of square waves as function of segments, and their values were compared with the percentage difference (Freqi XR-BK11/F - Freqi XR-BK11) / Freqi XR-BK11, in Figure 2B, where the apex i identifies the i-th segment. The average value frequency deviation was chosen on a random manner, with an average value of 4.0 ± 4.3. As shown in Figure 2A, B the visual comparison confirms that the XR-BK11/F sequence introduces only minor frequency shifts while preserving the broad spectral structure of the original sequence. The global energy content into the two sequences was reasonably the same because frequency deviations were small and measured field levels were very close.

XR-BK11 PEMF exposure reduced the expression of stemness-associated genes and neurosphere formation in glioblastoma cells

U87 cells were exposed to the XR-BK11 PEMF sequence once daily for four consecutive days. At the end of the treatment, viable cell number was quantified and total RNA was extracted for gene expression analysis. As shown in Figure 3A (phase-contrast photomicrographs at two magnifications) and Figure 3B, XR-BK11 exposure resulted in a modest reduction in cell number (approximately 15–20%). The expression of stemness-related genes was then analyzed in PEMF-exposed U87 cells. As shown in Figure 3C, XR-BK11 treatment significantly reduced the expression levels of *POU5F1* (encoding OCT4) and *NANOG*. Consistent with previous reports [45,46], *SOX2* expression was undetectable in untreated U87 cells and remained absent following PEMF exposure (data not shown). Notably, a significant decrease in *POU5F1* and *NANOG* expression was also observed in T98 cells after XR-BK11 exposure, despite no changes in cell number, (Figure S1A,B). In contrast, treatment with the XR-BK11/F sequence did not significantly affect U87 cell viability and produced only a modest reduction in the expression of these genes (Figure S2A-C).

XR-BK11 exposure did not alter the expression of *CD44* and *ALDH1A3* in U87 cells, but induced *CDH1* (encoding E-cadherin) expression (Figure 3C). To evaluate stem-like properties, a neurosphere assay was performed. U87 cells were exposed to the XR-BK11 PEMF sequence once daily for four days and then cultured under serum-free suspension conditions for an additional three

days. As shown in Figure 3E and F, XR-BK11 exposure reduced both the number and the size of the neurospheres.

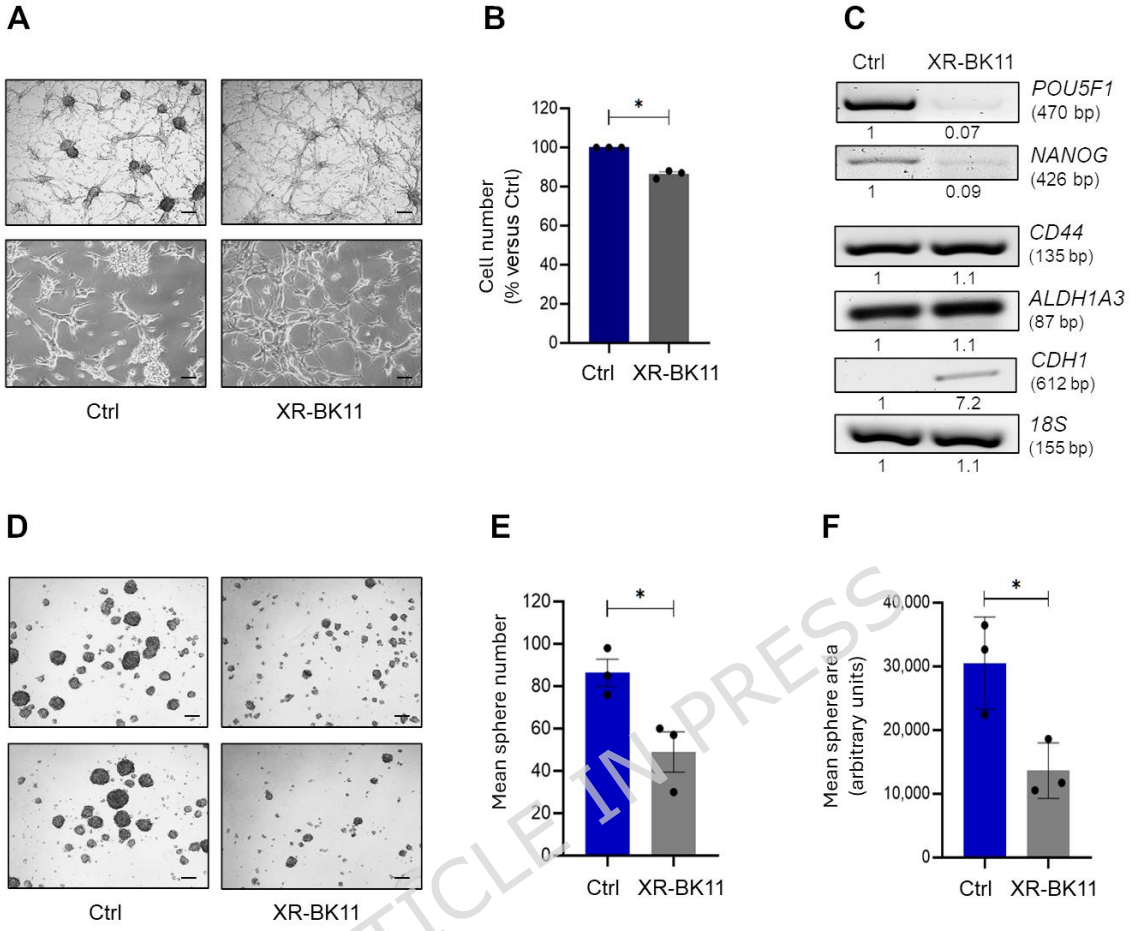

Figure 3. Effects of XR-BK11 PEMF sequence on U87 glioblastoma cell proliferation, gene expression and neurosphere formation capacity. (A) Representative phase-contrast photomicrographs of U87 cells, either untreated (Ctrl) of exposed to XR-BK11 PEMF sequence, captured at low and high magnification (x40 and x100) following four consecutive days of treatment. Scale bar=50µM. **(B)** Bar graph reporting the quantification of viable cells after four days of exposure to XR-BK11 PEMF sequence. Data are expressed as a percentage relative to untreated controls and represent mean ± SD from three independent experiments, *$p \leq 0.05$. **(C)** Representative mRNA expression levels of pluripotency-associated genes (*POU5F1*, *NANOG*) and mesenchymal-associated genes (*CD44, ALDH1A3* and *CDH1*) in U87 cells following XR-BK11 exposure, assessed by RT-PCR. 18S rRNA was used as housekeeping gene. Band intensities (Adj. Vol. int.) were quantified with Image Lab 5.2.1 (Bio-Rad). Data were normalized and reported as fold change relative to the control. **(D)** Representative phase-contrast photomicrographs of U87 glioblastoma cells cultured in suspension with the neurosphere medium for three days after exposure to XR-BK11 or untreated (Ctrl). Scale bar=50µM. Bar graphs reporting the sphere number. **(E)** and size **(F)** quantified as described in the Methods section. Data are expressed as a percentage relative to untreated controls and represent mean ± SD from three independent experiments, **** $p \leq 0.0001$.

PEMF exposure synergized with Temozolomide in inducing apoptotic death in glioblastoma cells

Temozolomide (TMZ) is the standard chemotherapeutic agent used in the treatment of GBM patients; however, drug resistance and undesirable side effects often hinder its clinical efficacy. A

promising therapeutic strategy for overcoming these challenges involves promoting cellular differentiation. To investigate the potential synergistic effects of PEMF combined with TMZ in GBM treatment, we treated U87 glioma cells with the PEMF sequence XR-BK11 once daily for four days, in the presence or absence of 200 µM TMZ. As shown by the phase-contrast photomicrograph in Figure 4A and the corresponding quantitative cell viability count in Figure 4B, the combined treatment of PEMF with TMZ significantly reduced cell viability respect to both treatments administered separately. Additionally, the increased in expression of the pro-apoptotic genes *BCL2L11* (encoding BIM) and *BBC3* (encoding PUMA), as illustrated in Figure 4C, along with the activation of Caspase 3, shown in Figure 4D, provide evidence that the combined therapy enhances apoptotic cell death in U87 cells. Similar results were observed in T98 cells (Figure S1B, C).

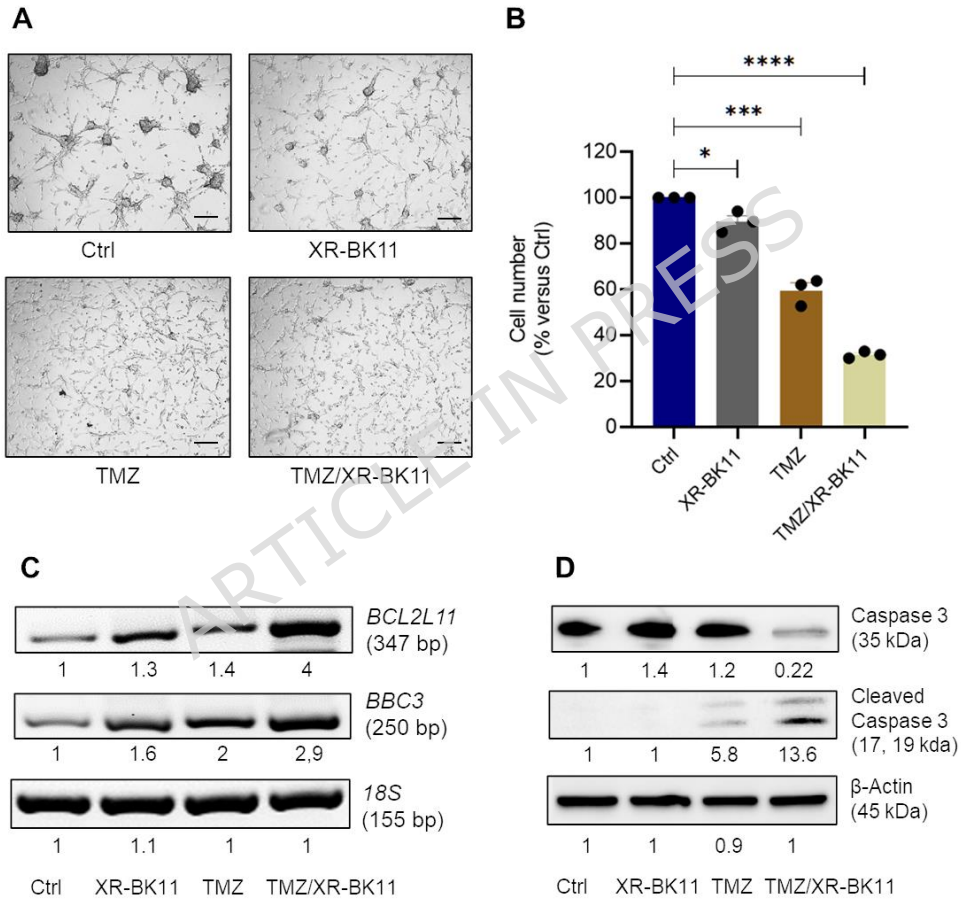

Figure 4. Synergistic effect of PEMF exposure and Temozolomide on U87 glioma cell viability and apoptosis. (A) Representative phase-contrast photomicrographs of U87 cells treated with PEMF sequence XR-BK11, 200 µM TMZ, and their combination for four consecutive days. Scale bar=50µM. **(B)** Bar graph reporting the U87 cell number not exposed and exposed once daily over four days to XR-BK11 PEMF sequence ± 200 µM TMZ. Data are expressed as a percentage relative to untreated controls and are presented as mean ± SD from three independent experiments, *$p \leq 0.05$, ***$p \leq 0.001$, ****$p \leq 0.0001$. **(C)** Relative mRNA expression levels of pro-apoptotic genes *BCL2L11* (encoding BIM) and *BBC3* (encoding PUMA) in U87 cells following PEMF and TMZ treatment. 18S rRNA was used as housekeeping gene. **(D)** Representative Western blot images showing Caspase 3 cleavage as a marker of apoptosis in U87 cells after treatment with PEMF sequence XR-BK11 ± 200 µM TMZ for four consecutive days. Band intensities (Adj. Vol. int.), in C and D, were quantified with Image Lab 5.2.1 (Bio-Rad). Data were normalized and reported as fold change relative to the control.

PEMF exposure did not affect the expression of stemness-related genes through modulation of AKT activation and synergized with AKT inhibition

AKT signaling is pivotal in regulating stemness and the biology of GSCs. To investigate the role of AKT activation in PEMF-mediated modulation of stemness-related genes, U87 cells were exposed to the PEMF sequence XR-BK11 once daily for four days. Western blot analysis (Figure 5A) revealed that XR-BK11 treatment did not alter the expression of AKT or its phosphorylation status (p-AKT). To further assess the impact of AKT signaling on stemness-related gene expression, U87 cells were co-treated with XR-BK11 and the AKT inhibitor MK-2206 (1 µM). Treatment with MK-2206 effectively inhibited AKT phosphorylation (Figure 5B) and downregulated the expression of *POU5F1* (encoding OCT4) and *NANOG* (Figure 5C). Interestingly, while XR-BK11 treatment did not affect p-AKT levels, it significantly decreased the expression of both *POU5F1* and *NANOG* (Figure 5C). To evaluate the potential synergistic effects on cellular proliferation of PEMF treatment with AKT inhibition, U87 cells were treated with XR-BK11 and MK-2206 simultaneously. As shown by phase-contrast photomicrographs (Figure 5D) and by cell viability bar graph (Figure 5E), the combined treatment resulted in a greater suppression of cell proliferation compared to either treatment alone. These results suggest that dual treatment with PEMF and AKT inhibitor may enhance therapeutic efficacy in targeting U87 cell propagation.

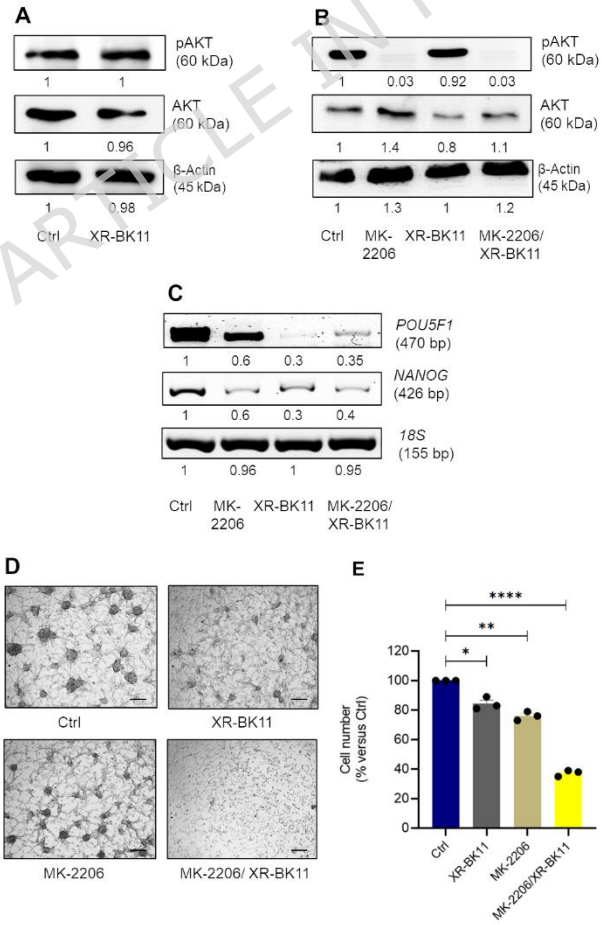

Figure 5. Effect of PEMF exposure and AKT inhibition on expression of stemness-related gene and U87 cell proliferation. **(A)** Representative Western blot images showing p-AKT and AKT expression levels in U87 cells treated with PEMF

sequence XR-BK11 for four consecutive days. β-Actin was used as loading control. **(B)** Representative Western blot images showing p-AKT and AKT expression levels in U87 cells treated with XR-BK11 in the presence or absence of 1 μM MK-2206. β-Actin was used as loading control **(C)** mRNA expression levels of stemness-related genes POU5F1 (encoding OCT4) and NANOG in U87 cells treated with XR-BK11 and/or MK-2206. 18S rRNA was used as housekeeping gene. Band intensities (Adj. Vol. int.), in A, B and C, were quantified with Image Lab 5.2.1 (Bio-Rad). Data were normalized and reported as fold change relative to the control. **(D)** Representative phase-contrast photomicrographs of U87 cells following treatment with XR-BK11, MK-2206, or their combination. Scale bar=50μM. **(E)** Quantification of U87 cell viability following treatment with XR-BK11, MK-2206, or their combination. Data are expressed as a percentage relative to untreated controls and represent mean ± SD from three independent experiments, * p≤0.05, **p≤0.01, ****p≤0.0001.

Discussion

The present study demonstrates that exposure of glioblastoma cells to the XR-BK11 PEMF sequence selectively modulates cellular plasticity and stem-like properties without inducing marked cytotoxic effects. In U87 cells, XR-BK11 treatment caused only a modest reduction in viable cell number, suggesting that the observed molecular and functional changes are not secondary to generalized growth inhibition or cell death, but rather reflect specific biological responses to PEMF exposure.

A key finding of this study is the significant downregulation of the core pluripotency regulators *POU5F1* (OCT4) and *NANOG* following XR-BK11 exposure. These transcription factors are critically involved in the maintenance of stemness and tumor-propagating capacity in glioblastoma, and their reduced expression is commonly associated with decreased cellular plasticity and impaired self-renewal. The consistent downregulation of these genes in both U87 and T98 cells, despite minimal effects on cell number, supports the notion that XR-BK11 preferentially targets stemness-associated transcriptional programs rather than overall cell viability.

XR-BK11 exposure did not alter the expression of *CD44* and *ALDH1A3*, two validated markers associated with mesenchymal identity in glioblastoma [47]. However, the concomitant upregulation of *CDH1* (E-cadherin gene) indicates the activation of epithelial-associated features, consistent with a partial mesenchymal-to-epithelial transition (MET). Such partial transitions have been described as intermediate cellular states that retain malignant traits while exhibiting reduced plasticity and stem-like potential.

Functional assays further support this interpretation. The reduction in both neurosphere number and size following XR-BK11 exposure indicates an impairment of clonogenic potential under stem cell–permissive conditions.

Notably, the XR-BK11/F sequence did not affect stemness gene expression and had no significant impact on cell viability, highlighting the sequence-specific nature of the biological response.

This observation supports the idea that distinct PEMF parameters can differentially engage intracellular signaling pathways, leading to selective modulation of gene expression programs.

Importantly, we observed in both cell lines a synergistic interaction between XR-BK11 PEMF exposure and TMZ, the first-line chemotherapeutic agent for GBM treatment in current clinical practices. The combination treatment significantly reduced cell viability and enhanced apoptosis, as

evidenced by increased expression of pro-apoptotic genes (*BCL2L11*/BIM and *BBC3*/PUMA) and activation of caspase-3. These effects support the hypothesis that diminishing cell stemness can enhance the efficacy of cytotoxic therapies.

Given the central role of the AKT signaling pathway in promoting glioma cell survival and maintaining stemness, we investigated whether the effects of XR-BK11 PEMF in U87 cells were mediated through AKT modulation. Surprisingly, our data indicate that PEMF exposure did not significantly alter total or phosphorylated AKT levels, suggesting that the regulatory effects on stemness gene expression occurred via an AKT-independent mechanism. However, when combined with MK-2206, a selective allosteric AKT inhibitor, XR-BK11 exposure led to downregulation of *POU5F1* and *NANOG*, as well as enhanced suppression of cell proliferation. This additive effect implies that PEMF may target distinct yet complementary pathways, involved in maintaining glioblastoma cell plasticity and proliferative capacity.

The observed ability of XR-BK11 PEMF to suppress stemness in two distinct GBM cell lines and synergize with both chemotherapeutic as well as targeted genes, positions this approach as a promising candidate for further preclinical development.

These findings raise important questions regarding the underlying molecular mechanisms, which remain to be elucidated, but it is evident that, rather than acting as direct cytotoxic agent, XR-BK11 appears to modulate the expression of key stemness regulators and a consequent increased responsiveness to standard chemotherapeutic agents. Interestingly, the lack of effect of XR-BK11/F on stemness-related gene expression and cell viability reinforces the concept that even minor deviations in frequency content prevent this biological response, suggesting that the waveform must be finely tuned [48].

Despite the limitations of in vitro GBM models, these findings offer a substantial contribution by characterizing frequency-specific effects on cancer stemness. This work provides the necessary framework for future studies to validate these mechanisms within in vivo environments, which more faithfully reflect the physiological complexities and heterogeneity of GBM.

Methods

Reagents and antibodies

The polyclonal antibodies specific for human AKT, p-AKT, Caspase 3 and β-Actin were purchased from Santa Cruz Biotechnology (Santa Cruz CA, USA). Anti-rabbit IgG peroxidase conjugated antibodies, MK-2206 and Temozolomide and other common reagents were from Merk Life Science S.r.l. (Milano, IT). ECL, nitrocellulose membranes and protein assay kit were from Bio-Rad Laboratories S.r.l. (Milano, IT). TRIzol, culture media and sera were from Thermo Fisher Scientific S.r.l. (Milano, IT).

Cell culture

The U87 and T98, human glioblastoma cell lines, from the American Type Culture Collection (ATCC, Rockville, MD), were grown in standard conditions in RPMI medium supplemented with 10% FBS

(Thermo Fisher Scientific S.r.l., Milano, IT), 100 µg/ml streptomycin and 10 µg/ml penicillin at 37°± 0.5° in a humidified environment containing 5% CO2.

Cell culture exposure to electromagnetic fields by means of SynthéXer

The U87 human glioblastoma cell line was grown in standard conditions in RPMI medium supplemented with 10% FBS, 100 µg/ml streptomycin and 10 µg/ml penicillin at 37°± 0.5° in a humidified environment containing 5% CO2. Cells were exposed 4 days, once a day, to pulsed electromagnetic fields by means of SynthéXer P/N E01S01025-01 (Ethidea Srl, Turin, Italy), a Class IIa medical device able to generate and deliver ultra-stable programmable signals with arbitrary waveform, in the frequency range from 10 Hz to 10 KHz, adapted for *in vitro* experiments [42]. A rectangular magnetic antenna was designed by means of FEM code (COMSOL Multiphysics®, www.comsol.it). The antenna was realized by a multiturn, single layer, copper wire solenoid 33 cm wide and 25 cm high, and was framed into the inner part of a plastic enclosure. The upper side of such antenna enclosure act as support for the flask containing the cells undergoing electromagnetic exposure. The solenoid into the enclosure is placed with its axis vertical so that the magnetic flux is perpendicular to the horizontal faces of the rectangular enclosure itself and it is driven by SynthéXer output signal. The “test volume” where the flasks are positioned is located around the central part of the upper face of rectangular enclosure, where the field distribution is uniform (Figure 6). The antenna was then located within the incubator with controlled temperature (37°± 0.5°) and 5% CO2. The exposure tests were carried out on cells samples following different paths: one sample was placed on the test region, and it was exposed to the defined sequence (SynthéXer ON). The corresponding sham exposed sample (Ctrl) was placed under the same conditions but with the solenoid radiating no field (SynthéXer OFF).

Before beginning the experiment and periodically during the tests, the magnetic flux density, as emitted from the device into the test region, was measured with a calibrated Electromagnetic Field Analyzer for monitoring low frequency fields (EFA-300, Narda Safety Test Solutions, www.narda-sts.com). Stray ambient AC fields were below 0.18 µT. The measured XR-BK11 magnetic flux emissions into the test region ranged from about 10 uT to 400 uT, over the whole operative wave segments. Instantaneous WM energy associated with those magnetic field levels can be expressed as a function of magnetic flux density (B), volume (Vol) and magnetic permeability, μ_O μ_R:

$$W_M = \frac{1}{2\mu_0\mu_R}|B|^2 \cdot (\mathrm{Vol}) \qquad (4)$$

where $\mu_O = 4\pi 10^{-7}$ H/m and $\mu_R \approx 1$ (4). Therefore, considering the volume of a cell of 10 µm radius, the range of energies associated with 10 µT to 400 µT magnetic flux of XR-BK11 is approximately equivalent from 0.7×10^{-21} J to 2.6×10^{-18} J.

It is intriguing to note that 10−19 Joules sets the scale of energies needed for bilayer bending by external forces [49]. For the sake of comparison, while the minimum value of applied field to which

a cell would respond without any selective, cooperative or amplifying mechanisms, was calculated to be about 1mV/cm for a large elongated cell and 20-40 mV/cm for a spherical cell [50], the peak values of the magnetically induced electrical field in our experimental setup fell in the μV/m range.

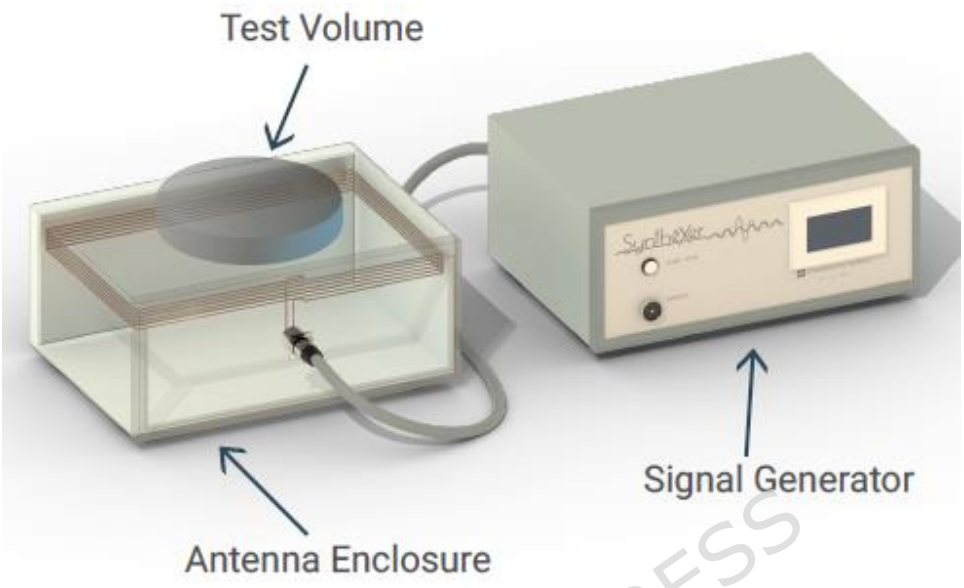

Figure 6. Laboratory set-up for electromagnetic exposure tests. A view of set-up for electromagnetic exposure tests. On the right side the SynthéXer programmable generator, connected by signal cable to the antenna unit, on the left side. The antenna, made by a rectangular and balanced copper multi-turn solenoid, is housed in a plastic enclosure. The cylindrical test region is on the upper face of the antenna unit enclosure.

Neurosphere formation assay

U87 cells cultured as monolayers, either exposed or unexposed to the XR-BK11 sequence, were detached, dissociated, and subsequently cultured in equal number in ultra-low attachment culture dishes. Cells were maintained in serum-free DMEM medium supplemented with EGF (20 ng/mL), FGF (10 ng/mL) and B27 supplement (Thermo Fisher Scientific S.r.l., Milano, IT) for an additional three days. Neurosphere number and size were quantified using the image analysis software Fiji/ImageJ, by converting images to 8-bit, applying thresholding, and utilizing Analyze > Analyze Particles to detect count and measure area.

Cell lysis and immunoblot

Proteins were extracted with 1% NP-40 lysis buffer (50 mM Tris-HCl pH 8.5 containing 1% NP-40, 150 mM NaCl, 10 mM EDTA, 10 mM NaF, 10 mM $Na_4P_2O_7$ and 0.4 mM Na_3VO_4) with freshly added protease inhibitors (10 μg/ml leupeptin, 4 μg/ml pepstatin and 0.1 Unit/ml aprotinin). Lysates were centrifuged at 13.000 x g for 10 minutes at 4° C and the supernatants were collected and assayed for protein concentration with the Bradford assay method (Bio-Rad Laboratories S.r.l.). Proteins were separated by SDS-PAGE under reducing conditions. Following SDS-PAGE, proteins were transferred to nitrocellulose, reacted with specific antibodies and then detected with peroxidase-conjugate secondary antibodies and chemioluminescent ECL reagent. Digital images were taken

with the Bio-Rad ChemiDocTM Touch Imaging System and quantified using Bio-Rad Image Lab 5.2.1.

RNA isolation and RT-PCR

Total RNA was extracted using TRIzol Reagent (Life-technologies), purified with chloroform and precipitated with isopropanol. Starting from equal amounts of RNA, cDNA used as template for amplification was synthesized by the reverse transcription reaction using RevertAid Minus First Strand cDNA Synthesis Kit from Bio-Rad Laboratories S.r.l. according to the manufacturer's instructions. 50 ng of cDNA were used to perform RT-PCR amplification of mRNA. For RT-PCR, template dilutions and/or differing numbers of PCR cycles were used to determine that PCR analysis was done within the linear range. PCR products were separated on a 1% agarose gel and stained with GelRed Nucleic Acid Gel Stain (Biotium, Fremont, CA). Digital images were taken with the Bio-Rad ChemiDocTM Touch Imaging System and quantified using Bio-Rad Image Lab 5.2.1.

Statistical analysis

Statistical analysis and data visualizations were performed in GraphPad Prism 8.0.2. All of data were expressed as the mean ± standard deviation (SD) of the results obtained from at least three independent experiments. Statistical evaluation of the differential analysis was performed by one-way ANOVA and Student's t-test. Differences with a p-level≤0.05 were considered significant.

References

1. Pouyan A., Ghorbanlo M., Eslami M., Jahanshahi M., Ziaei E., et al. Glioblastoma multiforme: insights into pathogenesis, key signaling pathways, and therapeutic strategies. *Mol. Cancer.* **24(1)**, 58 (2025).
2. Darlix A., Zouaoui S., Rigau V., Bessaoud F., Figarella-Branger D., et al. Epidemiology for primary brain tumors: a nationwide population-based study. *J. Neurooncol.* **131(3)**, 525-546 (2017).
3. Tang J., Amin M.A., Campian J.L. Glioblastoma Stem Cells at the Nexus of Tumor Heterogeneity, Immune Evasion, and Therapeutic Resistance. *Cells* **14(8)**, 562 (2025).
4. Wu W., Klockow J.L., Zhang M., Lafortune F., Chang E., et al. Glioblastoma multiforme (GBM): An overview of current therapies and mechanisms of resistance. *Pharmacol. Res.* **171**, 105780 (2021).
5. Tamimi A.F., Juweid M., De Vleeschouwer S., editors. Epidemiology and Outcome of Glioblastoma. (Glioblastoma [Internet]. Brisbane (AU): Codon Publications), **Chapter 8** (2017).
6. Tykocki T., Eltayeb M. Ten-year survival in glioblastoma. A systematic review. *J. Clin. Neurosci.* **54**, 7-13 (2018).
7. Agosti E., Antonietti S., Ius T., Fontanella M.M., Zeppieri M., et al. Glioma Stem Cells as Promoter of Glioma Progression: A Systematic Review of Molecular Pathways and Targeted Therapies. *Int J. Mol. Sci*. **25(14)**, 7979 (2024).
8. Ahmed A.U., Auffinger B., Lesniak M.S. Understanding glioma stem cells: rationale, clinical relevance and therapeutic strategies. *Expert. Rev. Neurother.* **13(5)**, 545-555 (2013).
9. Tang Z.Q., Ye Y.R., Shen Y. Molecular Mechanisms and Strategies for Inducing Neuronal Differentiation in Glioblastoma Cells. *Cell Reprogram.* **27(1)**, 24-32 (2025).
10. Rios Á.F.L., Tirapelli D.P.D.C., Cirino M.L.A., Rodrigues A.R., Ramos E.S., et al. Expression of pluripotency-related genes in human glioblastoma. *Neurooncol. Adv.* 2021 **4(1)**, vdab163.
11. Rodriguez R.T., Velkey J.M., Lutzko C., Seerke R., Kohn D.B., et al. Manipulation of OCT4 levels in human embryonic stem cells results in induction of differential cell types. *Exp. Biol. Med. (Maywood).* **232(10)**, 1368-1380 (2007).

12. Smith J., Field M., Sugaya K. Suppression of NANOG Expression Reduces Drug Resistance of Cancer Stem Cells in Glioblastoma. *Genes (Basel).* **14(6)**,1276 (2023).
13. Zając A., Sumorek-Wiadro J., Langner E., Wertel I., Maciejczyk A., et al. Involvement of PI3K Pathway in Glioma Cell Resistance to Temozolomide Treatment. *Int. J. Mol. Sci.* **22(10)**, 5155 (2021).
14. Madsen R.R. PI3K in stemness regulation: from development to cancer. *Biochem. Soc. Trans.* **48(1)**, 301-315 (2020).
15. Singh N., Miner A., Hennis L., Mittal S. Mechanisms of temozolomide resistance in glioblastoma - a comprehensive review. *Cancer Drug Resist.* **4(1)**,17-43 (2021).
16. Glaviano A., Foo A.S.C., Lam H.Y., Yap K.C.H., Jacot W., et al. PI3K/AKT/mTOR signaling transduction pathway and targeted therapies in cancer. *Mol. Cancer.* **22(1)**,138 (2023).
17. Chen L., Han L., Shi Z., Zhang K., Liu Yet al. LY294002 enhances cytotoxicity of temozolomide in glioma by down-regulation of the PI3K/Akt pathway. *Mol. Med. Rep.* **5(2)**, 575-579 (2012).
18. Zhao H.F., Wang J., Shao W., Wu C.P., Chen Z.P., To S.T., Li W.P. Recent advances in the use of PI3K inhibitors for glioblastoma multiforme: current preclinical and clinical development. *Mol. Cancer.* **16(1)**, 100 (2017).
19. Colardo M., Segatto M., Di Bartolomeo S. Targeting RTK-PI3K-mTOR Axis in Gliomas: An Update. *Int. J. Mol. Sci.* **22(9)**, 4899 (2021).
20. Zhao Q.W., Zhou Y.W., Li W.X., Kang B., Zhang X.Q., et al. Akt-mediated phosphorylation of Oct4 is associated with the proliferation of stem-like cancer cells. *Oncol. Rep.* **33(4)**, 1621-1629 (2015).
21. Lin Y., Yang Y., Li W., Chen Q., Li J., et al. Reciprocal regulation of Akt and Oct4 promotes the self-renewal and survival of embryonal carcinoma cells. *Mol. Cell.* **48(4)**, 627-640 (2012).
22. Panagopoulos D.J., Karabarbounis A., Margaritis L.H. Mechanism for action of electromagnetic fields on cells. *Biochem. Biophys. Res. Commun.* **298(1)**, 95-102 (2002).
23. Flatscher J., Pavez Loriè E., Mittermayr R., Meznik P., Slezak P., et al. Pulsed Electromagnetic Fields (PEMF)-Physiological Response and Its Potential in Trauma Treatment. *Int. J. Mol. Sci.* **24(14)**, 11239 (2023).
24. Ross C.L., Zhou Y., McCall C.E., Soker S., Criswell T.L. The Use of Pulsed Electromagnetic Field to Modulate Inflammation and Improve Tissue Regeneration: A Review. *Bioelectricity.* **1(4)**, 247-259 (2019).
25. Pantelis P., Theocharous G., Veroutis D., Vagena I.A., Polyzou A., et al. Pulsed Electromagnetic Fields (PEMFs) Trigger Cell Death and Senescence in Cancer Cells. *Int. J. Mol. Sci.* **25(5)**, 2473 (2024).
26. Funk R.H. Coupling of pulsed electromagnetic fields (PEMF) therapy to molecular grounds of the cell. *Am. J. Transl. Res.* **10(5)**, 1260-1272 (2018).
27. Ronniger M., Aguida B., Stacke C., Chen Y., Ehnert S., et al. A Novel Method to Achieve Precision and Reproducibility in Exposure Parameters for Low-Frequency Pulsed Magnetic Fields in Human Cell Cultures. *Bioengineering (Basel).* **9(10)**, 595 (2022).
28. Mansourian M., Shanei A. Evaluation of Pulsed Electromagnetic Field Effects: A Systematic Review and Meta-Analysis on Highlights of Two Decades of Research In Vitro Studies. *Biomed. Res. Int.* **2021**, 6647497 (2021).
29. Liu Y., Tang Q., Tao Q., Dong H., Shi Z., Zhou L. Low-frequency magnetic field therapy for glioblastoma: Current advances, mechanisms, challenges and future perspectives. *J. Adv. Res.* **69**,531-543 (2025).
30. Chiaramello E., Fiocchi S., Bonato M., Gallucci S., Benini M., et al. Cell transmembrane potential in contactless permeabilization by time-varying magnetic fields. *Comput. Biol. Med.* **135**, 104587 (2021).
31. Fröhlich H. Long-range coherence and energy storage in biological systems. *Int. J. of Quantum Chemistry* **2(5)**, 641-649 (1968).
32. Fröhlich H., Kremer F. Coherent Excitations in Biological Systems. *Ed. Springer-Verlag* (1983).

33. Tsong T.Y., Liu D.S., Chauvin F., Astuminan R.D. Resonance electroconformational coupling: a proposed mechanism for energy and signal transductions by membrane proteins. *Biosci. Rep.* **9(3)**,137-168 (1989).
34. Markin V.S., Tsong T.Y. Electroconformational coupling for ion transport in an oscillating electric field. *Bioelectrochem. Bioenerg.* **25(1)**,19-29 (1991).
35. Pall ML. Electromagnetic fields act via activation of voltage-gated calcium channels to produce beneficial or adverse effects. *J. Cell. Mol. Med.* **17**, 958-965 (2013).
36. Pasi F et al. Pulsed electromagnetic field with temozolomide elicits a pro-apoptotic effect with miRNA remodeling in T98G cells. *Anticancer Res.* **36**, 5821-5826 (2016).
37. Maioli, M.**,** Rinaldi, S., Pigliaru, G. et al. REAC technology and hyaluron synthase 2: an interesting network to slow down stem cell senescence. *Sci. Rep.* **6,** 28682 (2016).
38. Maioli, M.**,** Rinaldi, S., Migheli, R. et al. Neurological morphofunctional differentiation induced by REAC technology in PC12: a neuro-protective model for Parkinson's disease. *Sci. Rep.* **5,** 10439 (2015).
39. Yang C., Xu L., Liao F., Liao C., Zhao Y., et al. Pulsed electromagnetic fields regulate metabolic reprogramming and mitochondrial fission in endothelial cells for angiogenesis. *Sci. Rep.* **14**, 19027 (2024).
40. Sharpe M.A., Baskin D.S., Pichumani K., Ijare O.B., Helekar S.A. Rotating magnetic fields inhibit mitochondrial respiration and promote oxidative stress in cancer cells. *Front. Oncol.* **11,** 768758 (2021).
41. Hambarde S., Manalo J.M., Baskin D.S., Sharpe M.A., Helekar S.A. Spinning magnetic field patterns that cause oncolysis by oxidative stress in glioma cells. *Sci. Rep.* **13,** 19264 (2023).
42. Pinton G., Ferraro A., Balma M., Moro L. Specific low-frequency electromagnetic fields induce expression of active KDM6B associated with functional changes in U937 cells. *Electromagn. Biol. Med.* **39(2)**, 139-153 (2020).
43. Dixon J.R., Jung I., Selvaraj S., Shen Y., Antosiewicz-Bourget J.E., et al. Chromatin architecture reorganization during stem cell differentiation. *Nature* **518(7539)**, 331-336 (2015).
44. Martinsen O.G., Heiskanen A. Bioimpedance and Bioelectricity Basics. *Ed. Academic Pr.* (2023).
45. Lamour V., Henry A., Kroonen J., Nokin M.J., von Marschall Z., et al. Targeting osteopontin suppresses glioblastoma stem-like cell character and tumorigenicity in vivo. *Int. J. Cancer.* **137(5)**, 1047-1057 (2015).
46. Hong X., Chedid K., Kalkanis S.N. Glioblastoma cell line-derived spheres in serum-containing medium versus serum-free medium: A comparison of cancer stem cell properties. *Int. J. Oncol.* **41**, 1693-1700 (2012).
47. Wang Z., Zhang H., Xu S., Liu Z., Cheng Q. The adaptive transition of glioblastoma stem cells and its implications on treatments. *Signal. Transduct. Target Ther.* **6(1)**, 124 (2021).
48. Hu H, Yang W, Zeng Q, Chen W, Zhu Y, et al. Promising application of Pulsed Electromagnetic Fields (PEMFs) in musculoskeletal disorders. *Biomed. Pharmacother.* **131**,110767 (2020).
49. Graham T.R., Kozlov M.M. Interplay of proteins and lipids in generating membrane curvature. *Curr. Opin. Cell Biol*. **22(4)**, 430-436 (2010).
50. Santoro N., Lisi A., Pozzi D., Pasquali E., Serafino A., et al. Effect of extremely low frequency (ELF) magnetic field exposure on morphological and biophysical properties of human lymphoid cell line (Raji). *Biochim. Biophys. Acta* **1357(3)**, 281-290 (1997).

Author contributions

L.G. conducted the experiments on GBM cells, M.B. developed PEMF sequences, A.F., M.B., F.T., G.G. and G.P. contributed to data analysis and revised the manuscript, G.P. and L.M. designed the research and wrote the manuscript. L.M. funding acquisition. All authors contributed to this article and approved the submitted version.

Funding

This work was founded by the Fondazione Oncologica Valdostana (2024).

Competing interests

The authors declare no competing interests.

Data availability

The authors declare that the data supporting the findings of this study are available within the paper and its Supplementary Information files. Should any raw data files be needed in another format they are available from the corresponding author upon reasonable request.

Figure legends

Figure 1. Magnetic flux density associated with the XR-BK11 sequence segments and set of frequencies emitted during the 55-minute. (A) The general frame of SynthéXer signal is based on a series of N wave segments (N = 8 into the picture) where every segment holds a specific duration time. Within each segment several technical parameters such as frequency, waveform Xi, modulation and amplitude Ai are defined. **(B)** Measured magnetic field flux amplitude is shown versus the segment frequencies of the XR-BK11 sequence. The frequencies of the segments are sorted in order of emission. **(C)** This waterfall-like representation illustrates the complete set of frequencies emitted during the 55-minute XR-BK11 sequence, highlighting both the temporal and spectral distribution of the signal. Colour intensity and line thickness encode the frequency and harmonic rank, enhancing the visual perception of spectral density and structural coherence. This representation emphasizes how XR-BK11 systematically activates specific spectral bands over time, covering the biologically relevant α and β dispersion zones.

Figure 2. Comparison between XR-BK11 and XR-BK11/F frequences. **(A)** The bar plot shows the absolute frequencies used in the XR-BK11 sequence and its modified version XR-BK11/F, distributed across 11 time segments. Segments 1-6 correspond to the α/dispersion band (highlighted in blue background), while segments 7-11 harmonics fall within the β/dispersion band (highlighted in red background). **(B)** The plot illustrates the relative percentage differences between corresponding frequencies in the two sequences. Overall, the XR-BK11/F set maintains a close alignment to the original frequencies, with a mean deviation of 4.0% and a root-mean-square deviation of 4.3%. This visual comparison confirms that the XR-BK11/F sequence introduces only minor frequency shifts while preserving the broad spectral structure of the original sequence.

Figure 3. Effects of XR-BK11 PEMF sequence on U87 glioblastoma cell proliferation, gene expression and neurosphere formation capacity. (A) Representative phase-contrast photomicrographs of U87 cells, either untreated (Ctrl) of exposed to XR-BK11 PEMF sequence, captured at low and high magnification (x40 and x100) following four consecutive days of treatment. **(B)** Bar graph reporting the quantification of viable cells after four days of exposure to XR-BK11 PEMF sequence. Data are expressed as a percentage relative to untreated controls and represent mean ± SD from three independent experiments, $*p \leq 0.05$. **(C)** Representative mRNA expression levels of pluripotency-associated genes (*POU5F1*, *NANOG*) and mesenchymal-associated genes (*CD44, ALDH1A3* and *CDH1*) in U87 cells following XR-BK11 exposure, assessed by RT-PCR. 18S rRNA was used as housekeeping gene. Band intensities (Adj. Vol. int.) were quantified with Image Lab 5.2.1 (Bio-Rad). Data were normalized and reported as fold change relative to the control. **(D)** Representative phase-contrast photomicrographs of U87 glioblastoma cells cultured in suspension

with the neurosphere medium for three days after exposure to XR-BK11 or untreated (Ctrl). Bar graphs reporting the sphere number **(E)** and size **(F)** quantified as described in the Methods section. Data are expressed as a percentage relative to untreated controls and represent mean ± SD from three independent experiments, **** p≤0.0001.

Figure 4. Synergistic effect of PEMF exposure and Temozolomide on U87 glioma cell viability and apoptosis. (A) Representative phase-contrast photomicrographs of U87 cells treated with PEMF sequence XR-BK11, 200 µM TMZ, and their combination for four consecutive days. **(B)** Bar graph reporting the U87 cell number not exposed and exposed once daily over four days to XR-BK11 PEMF sequence ± 200 µM TMZ. Data are expressed as a percentage relative to untreated controls and are presented as mean ± SD from three independent experiments, *p≤0.05, ***p≤0.001, ****p≤0.0001. **(C)** Relative mRNA expression levels of pro-apoptotic genes *BCL2L11* (encoding BIM) and *BBC3* (encoding PUMA) in U87 cells following PEMF and TMZ treatment. 18S rRNA was used as housekeeping gene. **(D)** Representative Western blot images showing Caspase 3 cleavage as a marker of apoptosis in U87 cells after treatment with PEMF sequence XR-BK11 ± 200 µM TMZ for four consecutive days. Band intensities (Adj. Vol. int.), in C and D, were quantified with Image Lab 5.2.1 (Bio-Rad). Data were normalized and reported as fold change relative to the control.

Figure 5. Effect of PEMF exposure and AKT inhibition on expression of stemness-related gene and U87 cell proliferation. (A) Representative Western blot images showing p-AKT and AKT expression levels in U87 cells treated with PEMF sequence XR-BK11 for four consecutive days. β-Actin was used as loading control. **(B)** Representative Western blot images showing p-AKT and AKT expression levels in U87 cells treated with XR-BK11 in the presence or absence of 1 µM MK-2206. β-Actin was used as loading control **(C)** mRNA expression levels of stemness-related genes *POU5F1* (encoding OCT4) and *NANOG* in U87 cells treated with XR-BK11 and/or MK-2206. 18S rRNA was used as housekeeping gene. Band intensities (Adj. Vol. int.), in A, B and C, were quantified with Image Lab 5.2.1 (Bio-Rad). Data were normalized and reported as fold change relative to the control. (**D)** Representative phase-contrast photomicrographs of U87 cells following treatment with XR-BK11, MK-2206, or their combination. **(E)** Quantification of U87 cell viability following treatment with XR-BK11, MK-2206, or their combination. Data are expressed as a percentage relative to untreated controls and represent mean ± SD from three independent experiments, * p≤0.05, **p≤0.01, ****p≤0.0001.

Figure 6. Laboratory set-up for electromagnetic exposure tests. A view of set-up for electromagnetic exposure tests. On the right side the SynthéXer programmable generator, connected by signal cable to the antenna unit, on the left side. The antenna, made by a rectangular and balanced copper multi-turn solenoid, is housed in a plastic enclosure. The cylindrical test region is on the upper face of the antenna unit enclosure.